Performance and Lyapunov Stability of a Nonlinear Path-Following Guidance Method

Sanghyuk Park*
Bombardier Aerospace Corporation, Montreal, Quebec H9G 1M1, Canada
and
John Deyst† and Jonathan P. How‡
Massachusetts Institute of Technology, Cambridge, Massachusetts 02139

Performance and stability are demonstrated for a nonlinear path-following guidance method for unmanned air vehicles. The method was adapted from a pure pursuit-based path following, which has been widely used in ground based robot applications. The method is known to approximate a proportional-derivative controller when following a straight line path, but it is shown that there is also an element of anticipatory control that enables tight tracking when following curved paths. Ground speed is incorporated into the computation of commanded lateral acceleration, which adds an adaptive capability to accommodate vehicle speed changes due to external disturbances such as wind. Asymptotic Lyapunov stability of the nonlinear guidance method is demonstrated when the unmanned air vehicle is following circular paths. The adaptive nature of the guidance method makes its stability independent of vehicle velocity. The stability analysis is also extended to show robust stability of the guidance law in the presence of saturated lateral acceleration, which is an inherent limitation of flight vehicles. Flight tests of the algorithm, using two small unmanned air vehicles, showed that each aircraft was controlled to within 1.6 m root mean square when following circular paths. The method was used to perform a rendezvous of the two aircraft, bringing them into very close proximity, within 12 m of along track separation and 1.4 m root mean square relative position errors.

Nomenclature

$a_{s_{cmd}}$ = acceleration command sideways, that is, perpendicular to vehicle velocity direction
d = cross-track error
L_p = wavelength for a sinusoidal input path
L_1 = line segment defined from vehicle position to a reference point on the desired trajectory
R = radius of circle or circular segment that the aircraft is to follow
$S_{\dot\beta}$ = separation set on which $\dot\beta$ is identically zero
$S_{\dot\beta+\dot\eta}$ = separation set on which $\dot\beta + \dot\eta$ is identically zero
$S_{\dot\beta-\dot\eta}$ = separation set on which $\dot\beta - \dot\eta$ is identically zero
$S_{\dot\eta}$ = separation set on which $\dot\eta$ is identically zero
V = vehicle speed with respect to the ground
β = angle created from the velocity vector of the reference point to the line L_1, with clockwise positive
η = angle created from V to the line L_1, with clockwise positive

I. Introduction

TWO approaches can be considered for the problem of trajectory tracking. One method separates the vehicle guidance and control problems into an outer guidance loop and an inner control loop. The inner loop controls the vehicle so as to follow the acceleration commands generated by the outer loop. Simple strategies, based on geometric and kinematic properties, are typically used in the outer guidance loop. The alternative method uses an integrated approach wherein the inner and outer loops are designed simultaneously. In this case, a number of modern control design techniques can be applied, such as receding horizon [1], differential flatness [2,3], and neural network based adaptive controls [4].

In actual flight applications the separate inner and outer-loop approach is more commonly taken because it is usually simpler, and well-established design methods are available for inner-loop vehicle control. Linear controllers are commonly used for the outer-loop guidance of an aircraft. Typically proportional and derivative (PD) controllers are used to reduce the magnitude of the cross-track error, which is the lateral deviation from a desired flight path. If the desired trajectory path has gentle curvature, then this simple strategy will provide reasonably good outer-loop performance. However when tasks require tight tracking of complex curved paths, linear feedback on the cross-track error may not provide satisfactory performance.

There are several nonlinear approaches that have been proposed for unmanned vehicle trajectory tracking. In [5], Nelson et al. describe an approach using vector fields to represent desired ground track headings, so as to direct the vehicle onto the desired path. In [6], a Lyapunov approach is used to control the vehicle velocity vector to ensure convergence to a limit cycle. The method is well suited to guiding a vehicle from any initial position to a circular orbit above a target location. Reference [7] presents an approach that can accommodate large cross-track or heading deviations from a straight line path between waypoints. In contrast to the complexity of these approaches, the guidance law considered in this paper is very simple and easy to implement, and it has been effective in a very broad range of applications including ground rovers and unmanned air vehicles.

There are several terminal phase guidance laws that can be used to accomplish trajectory following by using an imaginary point moving along the desired flight path as a pseudotarget. Among these, pure pursuit guidance has been developed for ground rover path control [8–13] and has been widely used in robotic applications. The guidance method discussed in this paper adapts this method to create the lateral acceleration commands for controlling unmanned air vehicles (UAVs). Our analysis of this nonlinear guidance method

*Engineer, Fly-By-Wire; sanghyuk.park@aero.bombardier.com.
†Professor, Department of Aeronautics and Astronautics; deyst@mit.edu.
‡Associate Professor, Department of Aeronautics and Astronautics; jhow@mit.edu.

demonstrates a number of benefits over the other approaches for following curved paths. In particular, the nonlinear guidance law:

1) Naturally follows any circular path of radius greater than a specific limit imposed by the dynamics of the vehicle;

2) Has an element of anticipation of the desired flight path, enabling tight tracking of curved flight trajectories;

3) Incorporates instantaneous vehicle speed, adding an adaptive feature with respect to changes in vehicle ground speed caused by external disturbances, such as wind;

4) Is asymptotically stable, for all velocities, in the entire state space of useful initial conditions, and in the presence of saturation limits on lateral acceleration;

5) Is very simple and straightforward to apply in actual flight applications.

In what follows Sec. II describes basic properties and performance of the nonlinear guidance method. Section III introduces a particular choice of state variables in constructing a dynamic model for following a circular path, along with an associated linear analysis. Section IV presents asymptotic Lyapunov stability of the nonlinear guidance law. Robust stability in the presence of input saturation is illustrated in Sec. V using an approach similar to that taken in Sec. IV. Flight test results, showing excellent tracking performance, are given in Sec. VI. The nonlinear guidance law was implemented in two unmanned air vehicles in the Parent Child Unmanned Air Vehicle (PCUAV) Project [14] at MIT.

II.   Nonlinear Guidance Law

The approach presented here has been adapted from a pure pursuit based method [8,9]. A reference point on the desired path is designated and a lateral acceleration command is generated according to the direction of the reference point, relative to vehicle velocity. The reference point is on the desired path at a constant distance (L_1) forward of the vehicle, as shown in Fig. 1. The lateral acceleration command is determined by

$$a_{s_{cmd}} = 2 \frac{V^2}{L_1} \sin \eta \qquad (1)$$

Some significant properties of the guidance equation can be readily inferred from Fig. 1:

1) The direction of the acceleration depends on the sign of the angle between the L_1 line segment and the vehicle velocity vector. For example, if the reference point is to the right of the vehicle velocity vector, then the vehicle will be commanded to accelerate to the right, which is the case in Fig. 1. The guidance method will tend to align the vehicle velocity direction with the direction of the L_1 line segment.

2) If the vehicle is far away from the desired path, then the guidance method tends to rotate the velocity direction so as to approach the desired path at a large angle. On the other hand, if the vehicle is close to the desired path, then the guidance law rotates the velocity direction so as to approach the desired path at a small angle.

3) At each point in time a circular path can be defined that passes through the position of the reference point and the vehicle position, and which is tangent to the vehicle velocity vector; as indicated by the dotted circular line in Fig. 1. The acceleration command generated by Eq. (1) is equal to the centripetal acceleration required to follow this instantaneous circular segment. This is readily shown by noting that $L_1 = 2R \sin \eta$ so that the centripetal acceleration is $V^2/R = 2(V^2/L_1) \sin \eta \equiv a_{s_{cmd}}$. Hence the nonlinear guidance law will produce a lateral acceleration that is appropriate to follow a circle of any radius R that is consistent with the vehicle's capabilities (i.e., a sufficiently small turning radius).

Remark: In steering ground rovers the pure pursuit based method in [8,9] generates a command for trajectory curvature using $\gamma = (2/L_1^2)x$, where x is the lateral displacement to the reference point, which can be shown to equal $L_1 \sin \eta$. In this case, the resulting lateral acceleration is
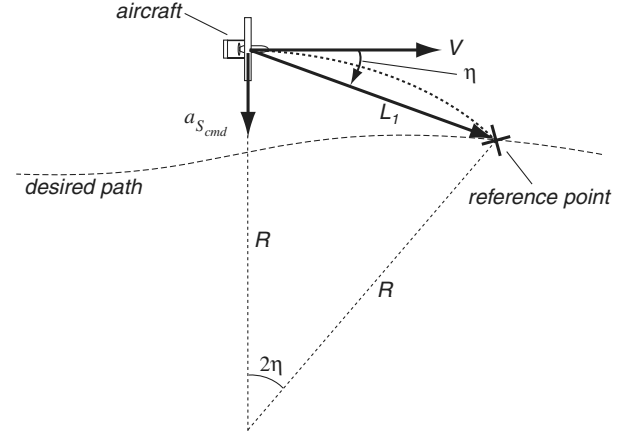

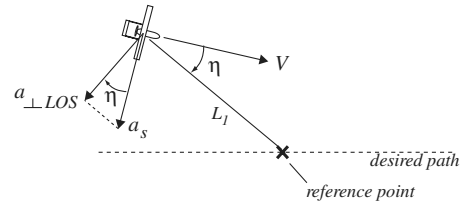Fig. 1   Diagram for the guidance law.

Fig. 2   Relation with proportional navigation.

$$a_s = V^2 \gamma = V^2 \left(\frac{2}{L_1^2} \right)(L_1 \sin \eta) = 2 \frac{V^2}{L_1} \sin \eta$$

which is equivalent to Eq. (1).

A.   Relation to Proportional Navigation Guidance Laws

There is an interesting similarity between this algorithm and the standard proportional navigation missile guidance approach if the reference point is considered a target. In particular, the lateral acceleration command in Eq. (1) can be shown to be equivalent to the formula for the acceleration command perpendicular to the line-of-sight in proportional navigation, with a navigation constant of $N' = 2$, under the assumption that the reference point is stationary in the computations of the line-of-sight rate and the closing velocity. This equivalence can be shown using Fig. 2 by noting that there is an angular difference between the vehicle lateral acceleration (a_s) and the acceleration perpendicular to the LOS. Using the acceleration command in Eq. (1) leads to

$$a_{\perp LOS} = a_s \cos \eta = 2 \frac{V^2}{L_1} \sin \eta \cos \eta = 2(V \cos \eta) \left(\frac{V}{L_1} \sin \eta \right)$$

Assuming that the target point is stationary, the first bracket is the closing velocity (the relative velocity component in the direction of the LOS) and the second bracket is the LOS rate. Therefore

$$a_{\perp LOS} = 2 V_C \dot{\lambda}$$

which is the form of the proportional navigation formula with the navigation constant equal to 2. However the similarity between the nonlinear guidance law and proportional navigation is only superficial because the reference point is actually moving along the reference trajectory and with L_1 constant the closing speed between the reference point and the vehicle is always zero.

B.   Linear Analysis and Frequency Response

An important design choice in the nonlinear guidance law is the look-ahead distance L_1 between the vehicle and the reference point. This value can be chosen with the help of a linear system analysis. When following a straight line path, the guidance law is known to
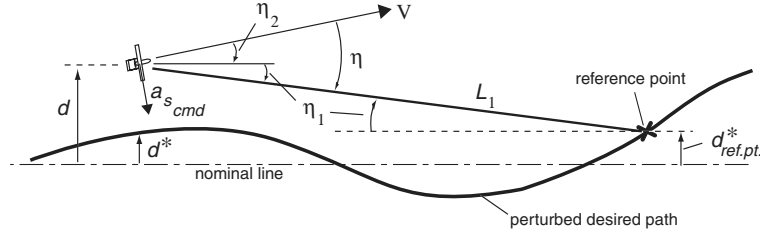
Fig. 3   Linear model for following a nonstraight perturbed line.

approximate a proportional-derivative controller [10]. Also a stability analysis is available in [9] with pure delay in the control loop, for straight paths and paths of constant curvature. This section presents linear analysis for following a curved path that is a perturbation from a nominal straight line.

Figure 3 defines the notation used in the linearization. The desired path is a small perturbation from a straight line, L_1 is the distance from the vehicle to the reference point on the desired path, and V is vehicle ground speed. Also d, $d^\star$, and $d^\star_{\text{ref pt}}$ are lateral perturbations of the vehicle, the desired path and the reference point from the nominal straight line, respectively. Assuming the magnitude of the angles, η_1 and η_2 are small

$$\sin \eta \approx \eta = \eta_1 + \eta_2 \qquad (2)$$

where $\eta_2 \approx \dot{d}/V$ and $\eta_1 \approx (d - d^\star_{\text{ref pt}})/L_1$. Combining these with the guidance formula, for the straight line case (i.e., $d^\star_{\text{ref pt}} = 0$) yields

$$a_{s_{\text{cmd}}} = 2\frac{V^2}{L_1}\sin \eta \approx 2\frac{V}{L_1}\left(\dot{d} + \frac{V}{L_1}d\right) \qquad (3)$$

which, as discussed in [10], shows that the linearization of the nonlinear guidance law produces a proportional plus derivative (PD) controller for the cross-track error, when following a straight line. Also vehicle speed V and look-ahead distance L_1 determine the proportional and derivative gains. For instance, a small value for L_1 leads to a high control gain and the ratio L_1/V determines the time constant of the PD controller. The distance L_1 can be chosen by performing a stability analysis with the linear plant model and the derived linear controller. The plant model should include the vehicle dynamics with inner-loop bank angle controller (if bank angle is used to generate lateral acceleration for the aircraft) and any sensor dynamics in the associated loop transmission function.

For the more general tracking problem with a perturbed trajectory (i.e., $d^\star_{\text{ref pt}} \neq 0$), note that for small perturbations $a_{s_{\text{cmd}}} \approx -\ddot{d}$, and applying Eqs. (1) and (2) gives

$$\ddot{d} + \frac{2V}{L_1}\dot{d} + \frac{2V^2}{L_1^2}d = \frac{2V^2}{L_1^2}d^\star_{\text{ref pt}} \qquad (4)$$

Taking the Laplace transforms of each term of Eq. (4) yields the input/output transfer function

$$\frac{d(s)}{d^\star_{\text{ref pt}}(s)} = \frac{\omega_n^2}{s^2 + 2\zeta\omega_n s + \omega_n^2} \quad \text{where } \zeta = 0.707,$$

$$\omega_n = \frac{\sqrt{2}V}{L_1} \qquad (5)$$

Equation (5) represents a second order low-pass linear system with a unity steady state gain from the reference point input to the vehicle position. The damping ratio (ζ) is always at the desirable 0.707 and the undamped natural frequency is $\omega_n = \sqrt{2}V/L_1$.

It is important to note that the input of the transfer function in Eq. (5) is the lateral position of the reference point, not the position of the desired path at the current vehicle location (i.e., $d^\star_{\text{ref pt}}$ not $d^\star$). In effect, the guidance law input comes from the reference point that is at the "look-ahead" distance L_1 ahead on the desired path. The use of a reference point ahead of the vehicle enables phase recovery around

the bandwidth frequency ω_n. Assuming that η is small, there is a time difference of approximately L_1/V between $d^\star$ and $d^\star_{\text{ref pt}}$ so that

$$\frac{d^\star_{\text{ref pt}}(s)}{d^\star(s)} \approx e^{\tau s}, \qquad \tau \approx L_1/V$$

Therefore Eq. (5) can be rewritten as

$$\frac{d(s)}{d^\star(s)} = \frac{\omega_n^2 e^{\tau s}}{s^2 + 2\zeta\omega_n s + \omega_n^2} \qquad (6)$$

To analyze this case further, consider a sinusoidal trajectory command written as

$$d^\star = A\sin\left(\frac{2\pi x}{L_p}\right) \qquad (7)$$

where A is a small path amplitude, L_p is the spatial wavelength of an input sinusoid (smaller values of L_p imply higher spatial frequencies), and x is distance along the path. Assuming $x \approx Vt$ produces an input frequency of $2\pi V/L_p$ and, recalling that $\omega_n = \sqrt{2}V/L_1$, gives the frequency response diagrams shown in Fig. 4. Then if the wavelength of the input is $L_p = \sqrt{2}\pi L_1 \approx 4.4L_1$, the commanded trajectory expressed by Eq. (7) will excite the system in Eq. (5) at the bandwidth frequency (ω_n) at which the phase lag is 90 deg. This is clearly shown in the Bode diagrams as a function of L_1/L_p in Fig. 4.

This phase lag is referenced from the position input of the reference point $d^\star_{\text{ref pt}}$, not from $d^\star$, in Fig. 3. Recalling that the reference point is at $L_1 = L_p/4.4$ (i.e., about a quarter period distance ahead) there will be about 90 deg of phase lead in $d^\star_{\text{ref pt}}$ over $d^\star$. Therefore the two effects tend to cancel each other, and the phase difference between the vehicle position and the desired path at the current vehicle location (i.e., between d and $d^\star$) will be significantly reduced. This is clearly shown in the Bode plot of Eq. (6) in Fig. 4, which illustrates the improvement in phase response near the system bandwidth (when $L_1/L_p \approx 1/4.4 = 0.23$) that results from the anticipation ($e^{\tau s}$).

Remark: This analysis indicates that if L_p is the wavelength of the highest frequency content in the desired path, then the look-ahead distance L_1 must be chosen to be less than about $L_p/4.4$ if the vehicle is to accurately follow the desired path. Furthermore both amplitude and phase are quite flat out to the system bandwidth frequency.

C. Comparison with Traditional Linear Methods

The previous section showed that for small perturbations about a straight line path the nonlinear guidance method approximates a linear PD controller operating on cross-track error. This section uses simulations to compare the performance of the nonlinear guidance law and the associated linear controller, for various cases of trajectories and wind conditions. For the linear controller in the simulation analysis presented below, a nominal vehicle speed of 25 m/s and a look-ahead distance (L_1) of 150 m were used to determine the fixed gains in the associated controller given by Eq. (3). When following a straight trajectory, the simulations, which are not shown here, indicate that the performances of the linear and nonlinear methods are virtually identical.
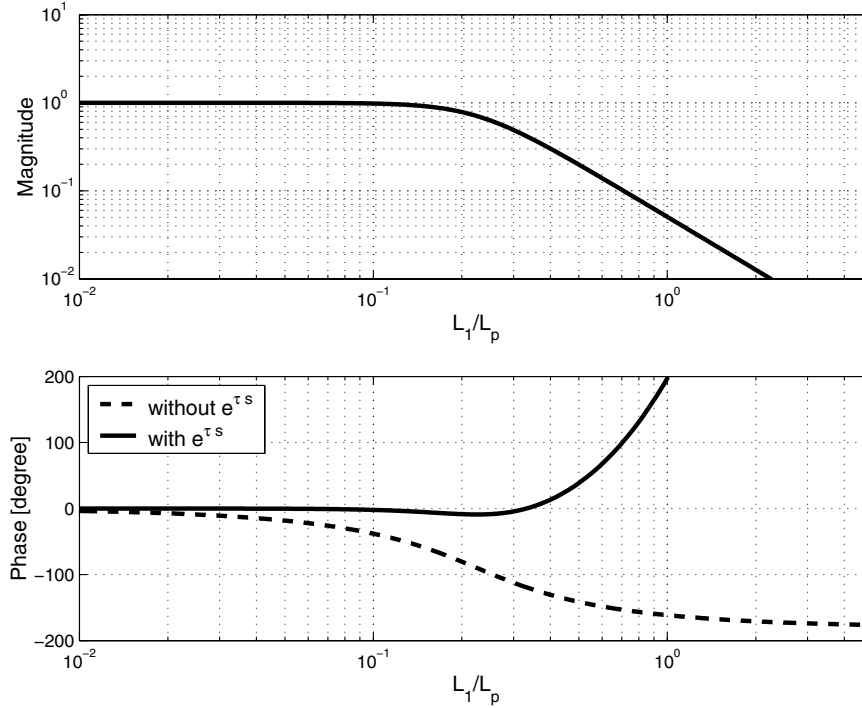
Fig. 4 Frequency response for guidance law.

1. Circular Trajectory Following with Wind

The two methods were applied to tracking a circle with a 5 m/s steady wind from west to east. Figure 5 shows the simulation setup, the desired curved flight trajectory, and the associated simulation results. The aircraft is initially heading due north. The performance of the linear controllers (PD and PID) are shown in the trajectory plot a) in Fig. 5. For the PD controller, the cross-track error varied in a range between 30 and 60 m, after the initial transition period. After an initial transient error of about 40 m the PID controller yielded a cross-track error that varied between ± 20 m after the initial transition period. A more careful look reveals that the vehicle flies outside the circular path when it is in the downwind region, and inside the circular path in the upwind region. The reason for this performance can be explained by noting that when the vehicle is in the downwind region, it moves faster with respect to an inertial frame. Under this condition, the vehicle must generate a larger acceleration command (or a larger bank angle command) if it is to follow the desired circular path. The linear feedback controller with fixed gain has an inherent limitation and cannot immediately remove the error, which is the result of inertial speed changes due to the wind.

On the other hand, the nonlinear guidance law method worked very well in following the curved path, in the presence of wind, as shown in Fig. 5b. The reason for the better performance in this case can be understood by the formula in Eq. (1) where the vehicle ground speed V is used at each instant in generating the acceleration command. In other words, the nonlinear guidance law takes into account the inertial velocity changes due to the wind effect, and adapts to the situation accordingly.

2. Linked Circular Path Following

As described in Sec. II, the nonlinear guidance law creates a centripetal acceleration required for the instantaneous circle defined by the reference point, vehicle position, and velocity direction. Therefore the nonlinear guidance law tends to have a cross-track error when the radius of the desired path changes or the turning direction is altered. To see this effect, simulations were performed for following linked circular paths as shown in Fig. 6. The commanded path is composed of five circular segments with the minimum radius being 250 m (i.e., $L_1 = 0.6R$) for the second, the third, and the fifth segments. For the PID linear controller, the peak cross-track error is

found to be near 70 m when following the second and the third circular segment. For the nonlinear guidance law, the peak error is found to be near 15 m when following from the second to the third circular segments.

Remark: Simulations, not shown here, demonstrated that gain-scheduling the PID controller with ground speed can significantly remove errors due to wind. However the error during the initial transient period, as shown in Fig. 5, still remains. In particular, when the commanded path has many changes of curvature, as shown in the example in Fig. 6, the system is in transition for much of the maneuver and overall performance of the PID controller is limited. In contrast, as shown in Fig. 6, the nonlinear guidance law performs much better because it is far less sensitive to transients, while still providing zero steady state error.

Remark: The adaptive velocity feature of the guidance method yields a demonstration of Lyapunov stability of the nonlinear controller that is independent of velocity, as shown in Sec. IV.

III. Analysis of the Nonlinear Guidance Method

It is important to study transient system behavior for situations where nonlinear effects are significant, which is typically the case when the initial vehicle state is far away from any stationary point representing the desired path. This section develops a state space model for following a circular path with the nonlinear guidance method. The model will be used in Sec. IV to demonstrate asymptotic Lyapunov stability and in Sec. V to investigate saturation effects.

A. Nonlinear State Space Model

Figure 7 illustrates the system geometry for a desired path that is circular. In the following development all angles and angular velocities are defined to be positive in the clockwise direction and it is assumed that the inner-loop control system produces the commanded acceleration exactly, so that a_s is equal to $a_{s_{cmd}}$. As shown in the figure, the vehicle velocity vector has a component $V_L = V \cos \eta$ along the line segment from the vehicle to the reference point, and a component $V_1 = V \sin \eta$ orthogonal to that line. Also because the reference point always lies on the desired path it must have a velocity vector V_T that is tangent to the path. Recalling that L_1 is a fixed length, the velocity of the reference point, in the direction of L_1, is $V_L = V_T \cos \beta$. Furthermore from the diagram in Fig. 7, the reference
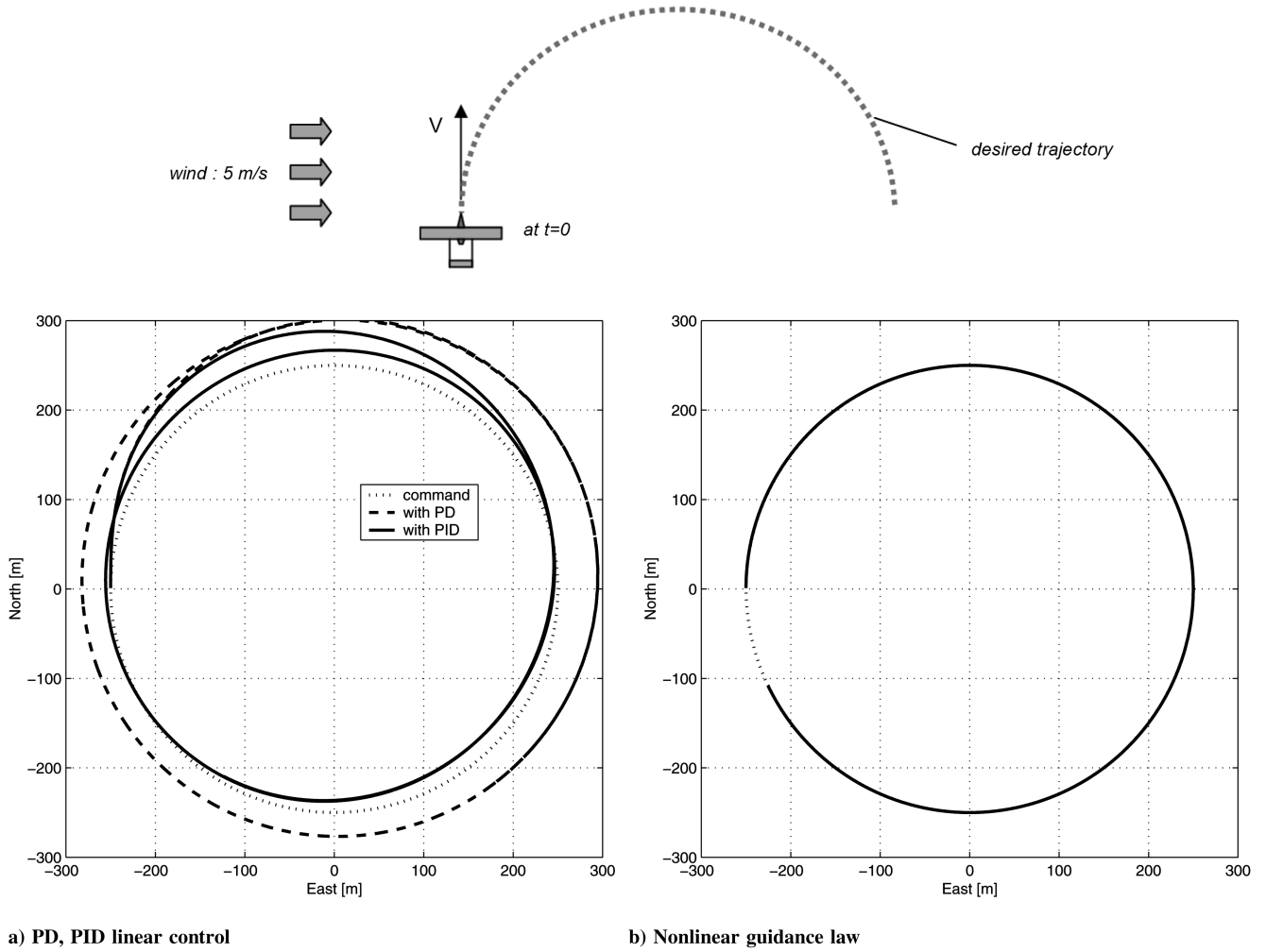
a) PD, PID linear control   b) Nonlinear guidance law

Fig. 5   Comparison: circle following with wind.
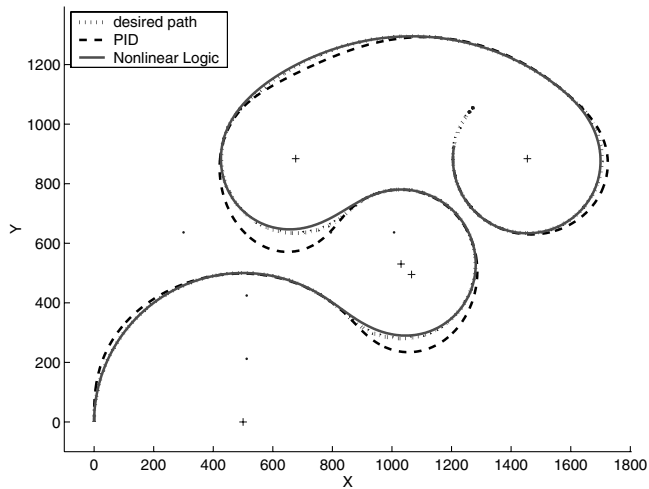
Fig. 6   Comparison: linked circular path following. Flight starts at the origin.

Fig. 7   System geometry for following circular paths.

From Fig. 7, the rates of change of the angles η and β can be expressed in terms of the inertial angular rotation rates ω_L, ω_V, and ω_T

$$\dot{\eta} = \omega_L - \omega_V \qquad \dot{\beta} = \omega_L - \omega_T \qquad (10)$$

Then with reference to Fig. 7, and using the above relations,

$$\omega_L = \frac{V_1 - V_2}{L_1} = \frac{V}{L_1}(\sin\eta - \cos\eta\tan\beta) \qquad \omega_T = \frac{V_T}{R} = \frac{V\cos\eta}{R\cos\beta} \qquad (11)$$

Also using Eq. (1)

point velocity orthogonal to L_1 is $V_2 = V_T \sin\beta$. Combining these relations gives

$$V_T = \frac{V_L}{\cos\beta} = \frac{V\cos\eta}{\cos\beta} \qquad (8)$$
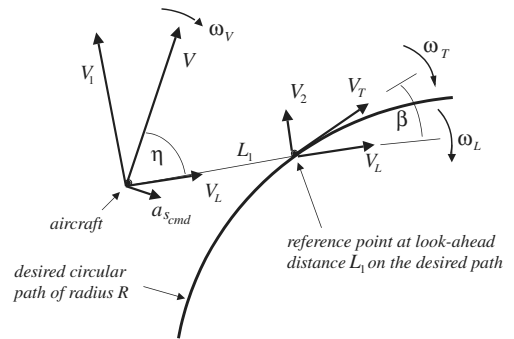
$$V_2 = V_T \sin\beta = V\cos\eta\tan\beta \qquad (9)$$

$$\omega_V = \frac{a_s}{V} = \frac{2V}{L_1} \sin \eta \qquad (12)$$

Substitution of Eqs. (11) and (12) into (11) yields

$$\dot{\eta} = -\frac{V}{L_1}(\sin \eta + \cos \eta \tan \beta) \qquad (13)$$

$$\dot{\beta} = \frac{V}{L_1}(\sin \eta - \cos \eta \tan \beta) - \frac{V \cos \eta}{R \cos \beta} \qquad (14)$$

which are the nonlinear differential equations for the two angles η and β, which are the system state variables. If the states always satisfy the conditions

$$|\eta(t)| < 90 \text{ deg} \qquad |\beta(t)| < 90 \text{ deg} \qquad (15)$$

then the differential equations are well behaved and satisfy Lipschitz conditions.

Remark: The following development will yield conditions on the relationship between the look-ahead distance and the circular radius to ensure satisfaction of these conditions. Also in what follows, the range of allowable initial states will be restricted as in Eq. (15). That condition applied to $\eta(0)$ specifies that the vehicle will approach the desired circular path such that the reference point is initially ahead of the vehicle. As well, the condition applied to $\beta(0)$ specifies that the approach will be such that the reference point will initially move along the desired path in the forward direction.

A unique stationary point for this system is obtained by first dividing Eq. (13) through by $\cos \eta$ and then setting $\dot{\eta} = 0$, which gives $\beta_0 = -\eta_0$. Using this condition and setting $\dot{\beta} = 0$ in Eq. (14) gives the stationary point

$$\eta_0 = \sin^{-1}\left(\frac{L_1}{2R}\right) = -\beta_0 \qquad (16)$$

which represents a perfect following of the desired circular path. The aircraft trails the reference point around the circle at a chord length L_1 behind the reference point. Indeed substitution of η_0 from Eq. (16) into the nonlinear guidance law defined in Eq. (1) yields the centripetal acceleration required to maintain the aircraft on the circle. Implicit in Eq. (16) is the condition $L_1 \le 2R$, which is necessary because the look-ahead distance cannot exceed the diameter of the circle to which the aircraft must converge.

B. Linearization About a Circular Trajectory

Using the stationary point in Eq. (16), a set of linear equations can be obtained for small perturbations from the circle. If $\Delta\eta$ and $\Delta\beta$ are small perturbations around the stationary point, so that $\eta = \eta_0 + \Delta\eta$ and $\beta = \beta_0 + \Delta\beta$, then Eq. (13) becomes

$$\Delta\dot{\eta} \approx -\frac{V}{L_1}\{(\cos \eta_o - \sin \eta_0 \tan \beta_0)\Delta\eta + (\cos \eta_0 \sec^2\beta_0)\Delta\beta\}$$

At the stationary point

$$\sin \eta_0 = -\sin \beta_0 = \frac{L_1}{2R}, \qquad \cos \eta_0 = \cos \beta_0 = \sqrt{1 - \left(\frac{L_1}{2R}\right)^2}$$

which, upon substitution, yields

$$\Delta\dot{\eta} \approx -\frac{V}{L_1\sqrt{1 - \left(\frac{L_1}{2R}\right)^2}}(\Delta\eta + \Delta\beta) \qquad (17)$$

Also Eq. (14) becomes

$$\Delta\dot{\beta} \approx \frac{V}{L_1}\left(\cos \eta_0 + \sin \eta_0 \tan \beta_0 + \frac{L_1}{R}\sin \eta_0 \sec \beta_0\right)\Delta\eta$$
$$- \frac{V}{R}\left(\frac{R}{L_1}\cos \eta_0\sec^2\beta_0 + \cos \eta_0 \sec \beta_0 \tan \beta_0\right)\Delta\beta \qquad (18)$$

Substituting for η_0 and β_0 at the stationary point gives

$$\Delta\dot{\beta} \approx \frac{V}{L_1\sqrt{1 - (\frac{L_1}{2R})^2}}\left[\Delta\eta + \left\{2\left(\frac{L_1}{2R}\right)^2 - 1\right\}\Delta\beta\right] \qquad (19)$$

Equations (17) and (19) represent a second order system, where the associated undamped natural frequency and the damping ratio are

$$\omega_n = \frac{\sqrt{2}V}{L_1}, \qquad \zeta = \frac{1}{\sqrt{2}}\sqrt{1 - \left(\frac{L_1}{2R}\right)^2} \qquad (20)$$

Comparing with Eq. (5) for the straight line case, Eqs. (20) indicate that the damping ratio is modified for the circular path case as a function of the ratio L_1/R while the undamped natural frequency remains unchanged.

IV. Asymptotic Lyapunov Stability

The purpose of this section is to use the model developed in Sec. III.A to create a Lyapunov function that ensures stability of the nonlinear guidance law when the desired path is circular. The stability for a straight path is the special case when R approaches infinity.

A. Bounds on State Derivatives

Much of the development in this section builds on the results of Blanchini [15]. First consider the regions in the state space where the derivatives of state variables go to zero. For example the set of states where $\dot{\eta}$ equals zero can be obtained by the same procedure used to obtain Eq. (16). Dividing both sides of Eq. (13) by $\cos \eta$ and setting $\dot{\eta}$ to zero yields

$$\dot{\eta} = 0 \Leftrightarrow \eta = -\beta \qquad (21)$$

and by inspection of Eq. (13)

$$\dot{\eta} > 0 \Leftrightarrow \eta < -\beta \qquad (22)$$

$$\dot{\eta} < 0 \Leftrightarrow \eta > -\beta \qquad (23)$$

Figure 8 depicts these conditions in the two-dimensional state space. The conditions partition the space into two regions separated by the diagonal line of points that are elements of the separation set $S_{\dot{\eta}}$ where

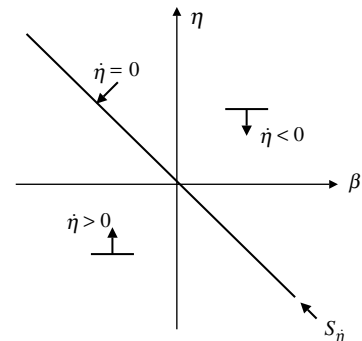$$S_{\dot{\eta}} = \{\eta, \beta : \eta = -\beta\} \qquad (24)$$

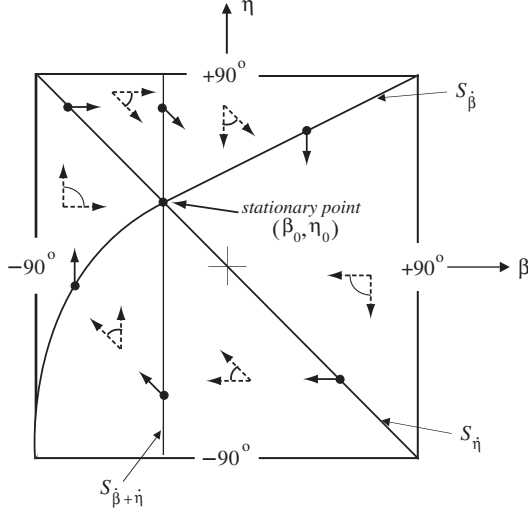**Fig. 8   Conditions on $\dot{\eta}$.**

Fig. 9 Intersection of the conditions on state trajectories.

Similar conditions on $\dot{\beta}$ are realized by multiplying both sides of Eq. (14) by $\cos\beta/V$ and setting $\dot{\beta}$ to zero obtaining

$$(\sin\eta\cos\beta - \cos\eta\sin\beta) = \sin(\eta - \beta) = \frac{L_1\cos\eta}{R} \quad (25)$$

which yields the condition

$$\dot{\beta} = 0 \Leftrightarrow \beta = \eta - \sin^{-1}\left(\frac{L_1\cos\eta}{R}\right) \quad (26)$$

and inspection of Eq. (14) produces

$$\dot{\beta} > 0 \Leftrightarrow \beta < \eta - \sin^{-1}\left(\frac{L_1\cos\eta}{R}\right) \quad (27)$$

$$\dot{\beta} < 0 \Leftrightarrow \beta > \eta - \sin^{-1}\left(\frac{L_1\cos\eta}{R}\right) \quad (28)$$

The boundary between these two conditions in the two-dimensional state space is shown in Fig. 9. The state space is partitioned into two regions separated by the set $S_{\dot{\beta}}$ where

$$S_{\dot{\beta}} = \left\{\eta, \beta: \beta = \eta - \sin^{-1}\left(\frac{L_1\cos\eta}{R}\right)\right\} \quad (29)$$

The definition of $S_{\dot{\beta}}$ assumes that $L_1/R \leq 1$, which is necessary to ensure that Lipschitz conditions are always satisfied for all state space trajectories, especially when the initial state places the aircraft inside the circle.

A third set of useful conditions is obtained by considering the sum of the two state derivatives. In particular, adding Eqs. (13) and (14) produces

$$\dot{\beta} + \dot{\eta} = -\frac{2V\cos\eta}{L_1\cos\beta}\left(\sin\beta + \frac{L_1}{2R}\right) \quad (30)$$

Because both cosine terms in Eq. (30) are positive everywhere in the state space only the sine term in Eq. (30) can affect a sign change in $\dot{\beta} + \dot{\eta}$. Hence with reference to Eq. (16), the following conditions are realized:

$$\dot{\beta} + \dot{\eta} = 0 \Leftrightarrow \beta = -\sin^{-1}\left(\frac{L_1}{2R}\right) = \beta_0 \quad (31)$$

$$\dot{\beta} + \dot{\eta} > 0 \Leftrightarrow \beta < \beta_0 \quad (32)$$
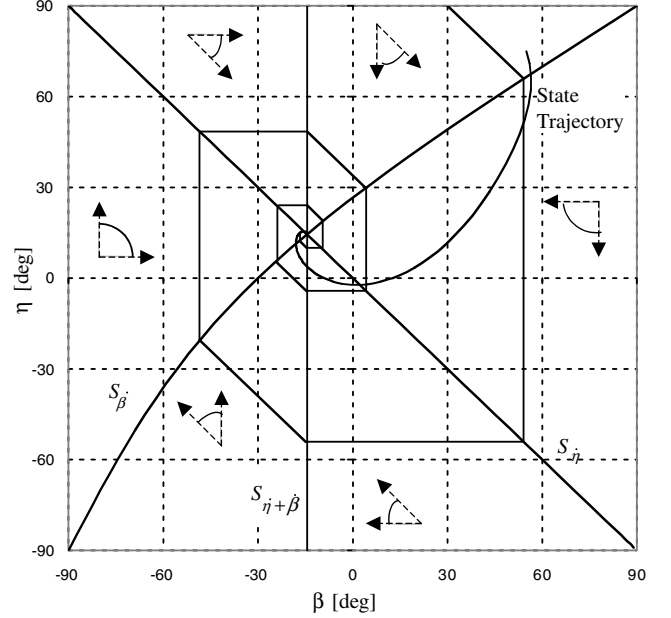

Fig. 10 Separation sets, convergent contour, and sample state trajectory for $L_1/R = 0.5$.

$$\dot{\beta} + \dot{\eta} < 0 \Leftrightarrow \beta > \beta_0 \quad (33)$$

Figure 9 shows how the state space is partitioned by the separation set $S_{\dot{\beta}+\dot{\eta}}$ where

$$S_{\dot{\beta}+\dot{\eta}} = \{\eta, \beta: \beta = \beta_0\} \quad (34)$$

Taken together all of these conditions impose restrictions on the directions that state trajectories can take in various regions of the state space. These regions are determined by the three separation sets $S_{\dot{\eta}}$, $S_{\dot{\beta}}$, and $S_{\dot{\beta}+\dot{\eta}}$.

Figure 9 is a representative diagram illustrating the composite or intersection of these conditions. The arrows in the figure indicate the possible directions that state trajectories can take both on the separation sets and inside each region, bounded by the separation sets and the periphery of the state. Inside each region the direction of state trajectories can only lie between the two associated arrows in dotted lines. The dotted arrows are used here to emphasize that the ranges of possible directions exclude the directions of the arrows themselves (i.e., the ranges of directions are open sets).

Note that because all state trajectories initiate strictly inside the state space they cannot cross the periphery of the state, and so the conditions on state trajectory directions verify the assumptions implicit in Eq. (15). Also both state derivatives are zero at the stationary point so that it must be an element of all three separation sets, as shown in Fig. 9. Furthermore as indicated by the arrows in the figure, state trajectories must proceed in a more or less clockwise fashion around the stationary point.

B. System Stability

Because the differential equations for the state variables satisfy Lipschitz conditions, all state trajectories will be continuous everywhere in the state space. In particular, the state trajectories must be continuous at points where they intersect the separation sets $S_{\dot{\eta}}$, $S_{\dot{\beta}}$, and $S_{\dot{\beta}+\dot{\eta}}$. Furthermore the conditions imposed on state trajectories must be consistent across the separation sets. Thus a contour composed of piecewise straight line segments can be constructed in the state space, as shown in Fig. 10.

The contour is continuous everywhere and the geometry of the separation sets ensures that it converges, in clockwise fashion, to the stationary point. The convergent contour, and the allowable state trajectory directions, are everywhere consistent with the conditions derived earlier, as illustrated in Fig. 9. Figure 10 is an accurate

representation of the separation sets for the particular case when the look-ahead distance is half the radius of the desired circle, and so $L_1/R = 0.5$. Thus for this specific case, the stationary point is located at $\eta_0 = -\beta_0 = 14.48$ deg and the three separation sets are

$$S_{\dot{\eta}} = \{\eta, \beta : \beta = -\eta\} \tag{35}$$

$$S_{\dot{\beta}} = \left\{\eta, \beta : \beta = \eta - \sin^{-1}\left(\frac{\cos\eta}{2}\right)\right\} \tag{36}$$

$$S_{\dot{\beta}+\dot{\eta}} = \{\eta, \beta : \beta = -14.48 \text{ deg}\} \tag{37}$$

Also as can be seen in Fig. 10, the contour proceeds in a clockwise fashion around the stationary point and converges to the stationary point. More generally, any such contour, emanating from any point in the state space, will converge to the stationary point. Furthermore as indicated by the arrows in Fig. 9, as a state trajectory evolves it must always cross a convergent contour from the left of the contour to right. Thus because all contours converge to the stationary point in the clockwise direction, all state trajectories must also converge to the stationary point in clockwise fashion. The sample state trajectory shown in Fig. 10 illustrates this clockwise convergence to the stationary point.

Small modifications of the convergent contour in Fig. 10 will serve to create a Lyapunov function. As shown in Fig. 11, closed polygons can be created by extending the descending vertical line segments of the convergent contour until they intersect either another line segment of the contour or reach the boundary of the state space. Although the smaller polygons in the space are completely formed by convergent contour line segments and their extensions, the larger polygons may be partially formed by line segments and their extensions, and partially formed by the boundaries of the state space.

The Lyapunov function can now be defined by construction. From every point in the state space the convergent contour that emanates from that point is constructed, as in Fig. 10. Clearly many points will share the same convergent contour. Then the closed polygons for each contour are constructed, yielding nested polygons, as shown in Fig. 11. The Lyapunov function at each point in the space is then defined as the area of the smallest polygon containing that point. Thus at each point on the periphery of a polygon the value of the Lyapunov function is constant and the periphery of the polygon is a level surface of the Lyapunov function.

By recalling Fig. 9, note that all state trajectories in Fig. 11 must pass from the exterior to the interior of every polygon except on the separation sets $S_{\dot{\beta}}$, $S_{\dot{\eta}}$, and $S_{\dot{\beta}+\dot{\eta}}$, where the state trajectory may lie instantaneously along an edge of the polygon. Therefore because trajectories always pass from larger to smaller nested polygons, their

area will decrease everywhere, except possibly on the separation sets. In other words the time derivative of the Lyapunov function is negative semidefinite. However asymptotic stability can be shown by La Salle's theorem [16]. The set

$$E \equiv \text{union of the separation sets} = \bigcup\{S_{\dot{\eta}}, S_{\dot{\beta}}, S_{\dot{\eta}+\dot{\beta}}\}$$

contains all points where the time derivative of the Lyapunov function becomes zero. The stationary point at η_0, β_0 is unique and it lies in E, and so it is the largest invariant set in E. Thus by La Salle's theorem, every solution will be asymptotically stable.

A similar approach can be used to demonstrate stability on circular paths of different radii in the allowable range. The same approach can also be used to show stability for a straight line path and for the smallest allowable circular path as well, namely $L_1/R \to 0$ and $L_1/R \to 1$. Note that this demonstration of stability is completely dependent on the separation sets $S_{\dot{\eta}}$, $S_{\dot{\beta}}$, and $S_{\dot{\beta}+\dot{\eta}}$, all of which are independent of vehicle velocity. Hence the guidance method is asymptotically Lyapunov stable for all vehicle velocities.

A plan view simulation of the aircraft converging to the desired paths is shown in Fig. 12 which plots the aircraft path (dark line), and the desired circular path (circle), both of which are continuous lines. The figure also shows the instantaneous discrete positions of the look-ahead lines (L_1). At the beginning of each trajectory these lines are shown at equal increments of time (gray). The specific aircraft path shown in Fig. 12 corresponds to the η, β state trajectory shown in Figs. 10 and 11.

V. Saturation Effects

This section discusses the behavior of the nonlinear guidance law in the presence of saturation. In particular, if the available acceleration is limited by $|a_s| \leq a_s^*$, then a corresponding η^* limit can be defined as

$$\eta^* = \sin^{-1}\left(\frac{a_s^* L_1}{2V^2}\right) \tag{38}$$

To accommodate the saturation limit in the system dynamics, Eqs. (10) and (11) remain unchanged, but Eq. (12) is modified to

$$\omega_V = \frac{a_s}{V} = \begin{cases} \frac{2V}{L_1}\sin\eta & \text{if } |\eta| \leq \eta^* \\ \frac{2V}{L_1}\text{sgn}(\eta)\sin\eta^* & \text{if } |\eta| > \eta^* \end{cases} \tag{39}$$

where

$$\text{sgn}(\eta) = \begin{cases} 1 & \eta \geq 0 \\ -1 & \eta < 0 \end{cases}$$

which gives the modified state equations

$$\dot{\beta} = \frac{V}{L_1}(\sin\eta - \cos\eta\tan\beta) - \frac{V\cos\eta}{R\cos\beta} \qquad \dot{\eta} = \begin{cases} -\frac{V}{L_1}(\sin\eta + \cos\eta\tan\beta) & \text{if } |\eta| \leq \eta^* \\ -\frac{V}{L_1}(2\text{sgn}(\eta)\sin\eta^* - \sin\eta + \cos\eta\tan\beta) & \text{if } |\eta| > \eta^* \end{cases} \tag{40}$$

The approach in Sec. IV can then be used to derive separation sets $S_{\dot{\beta}}$, $S_{\dot{\eta}}$, $S_{\dot{\beta}+\dot{\eta}}$, and $S_{\dot{\beta}-\dot{\eta}}$ corresponding to the conditions $\dot{\beta} = 0$, $\dot{\eta} = 0$, $\dot{\beta} + \dot{\eta} = 0$, and $\dot{\beta} - \dot{\eta} = 0$, respectively.

$$S_{\dot{\beta}} = \left\{\eta, \beta : \beta = \eta - \sin^{-1}\left(\frac{L_1\cos\eta}{R}\right)\right\} \qquad S_{\dot{\eta}} = \left\{\eta, \beta : \begin{cases} \eta = -\beta & \text{if } |\eta| \leq \eta^* \\ \tan\beta = \frac{\sin\eta - 2\,\text{sgn}(\eta)\sin\eta^*}{\cos\eta} & \text{if } |\eta| > \eta^* \end{cases}\right\}$$

$$S_{\dot{\beta}+\dot{\eta}} = \left\{\eta, \beta : \begin{cases} \beta = \beta_0 = -\sin^{-1}\left(\frac{L_1}{2R}\right) & \text{if } |\eta| \leq \eta^* \\ \sin\eta - \text{sgn}(\eta)\sin\eta^* - \frac{\cos\eta}{\cos\beta}\left(\sin\beta + \frac{L_1}{2R}\right) = 0 & \text{if } |\eta| > \eta^* \end{cases}\right\} \qquad S_{\dot{\beta}-\dot{\eta}} = \left\{\eta, \beta : \begin{cases} \cos\beta = \frac{L_1\cos\eta}{2R\sin\eta} & \text{if } |\eta| \leq \eta^* \\ \cos\beta = \frac{L_1\cos\eta}{2R\,\text{sgn}(\eta)\sin\eta^*} & \text{if } |\eta| > \eta^* \end{cases}\right\} \tag{41}$$
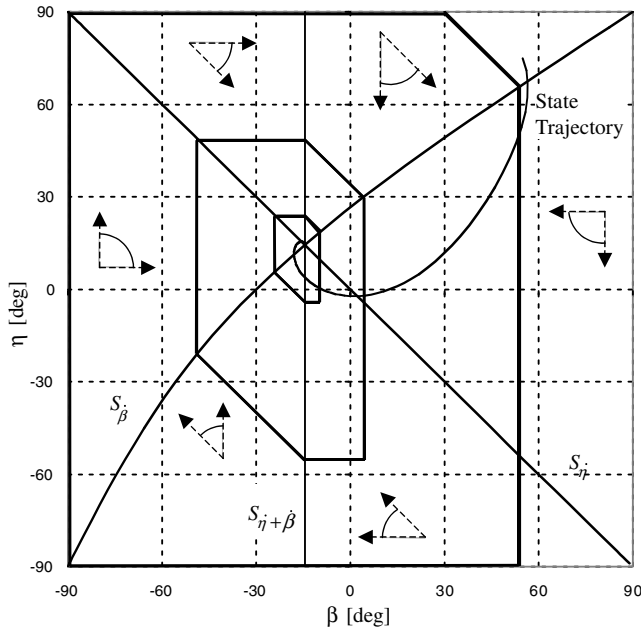
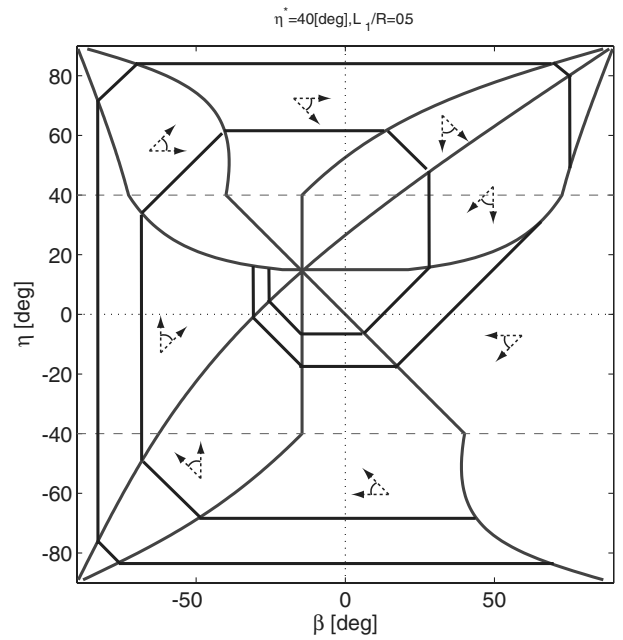Fig. 11 Separation sets, Lyapunov polygons, and sample state trajectory for $L_1/R = 0.5$.

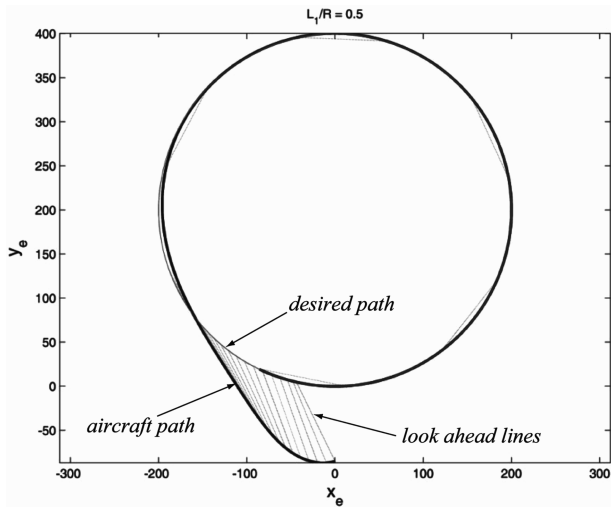Fig. 13 Separation sets and convergent boundary contour.

Fig. 12 Simulation of aircraft converging to a circle ($L_1/R = 0.5$).

Fig. 14 Phase plot.

For comparison, the separation sets for a case when $\eta^* = 40$ deg with $L_1/R = 0.5$ are shown in Fig. 13, which can be compared with the equivalent unsaturated case in Fig. 10. The figure also shows the possible directions of the trajectory at each region made by the separation sets and the associated convergent contours. Note that the shapes of the separation sets are distorted for the region where $|\eta| > \eta^*$. The plot shows that the contours converge to the stationary point, and the associated phase plot in Fig. 14 shows convergence throughout the entire state space defined by $|\eta| < 90$ deg and $|\beta| < 90$ deg.

For lower saturation levels (i.e., smaller η^*) the convergence region is reduced. In particular, there is a drastic change in the shape of the separation sets, especially for $S_{\dot{\eta}}$ in Eq. (41), when $\eta^* \approx 30$ deg. Figure 15 shows the separation sets and the phase plot for $\eta^* = 25$ deg as an example case of $\eta^* < 30$ deg. In the regions created by $S_{\dot{\eta}}$ and $S_{\dot{\beta}-\dot{\eta}}$ when $|\eta|$ is relatively close to 90 deg, the possible directions of state trajectories, as indicated by the arrows and the associated angles in Fig. 15, will make $|\eta|$ even larger. Therefore some of the trajectories with relatively large $|\eta|$ values will exit the state space, as shown in Fig. 15. These results show that it is only possible to use the techniques of Sec. IV to show that the entire region is convergent when $\eta^* < 30$ deg.
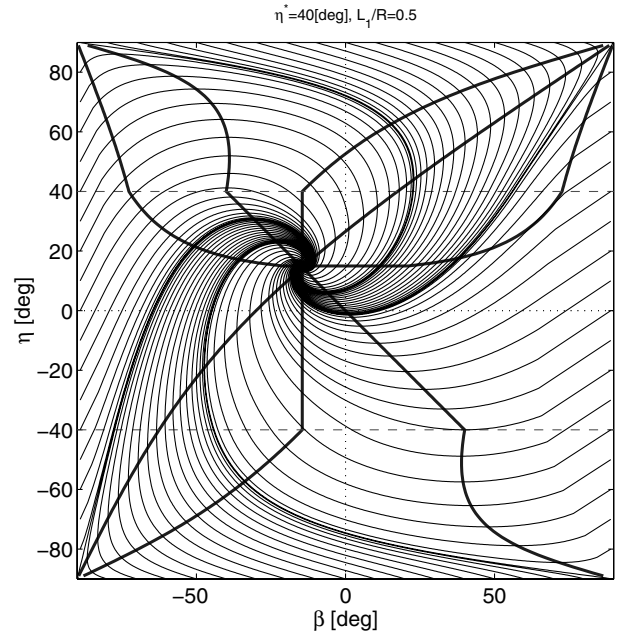
In conclusion, as long as the available acceleration is greater than the centripetal acceleration required to follow a circular path of radius L_1, that is $\eta^* = 30$ deg, the entire region defined by $|\eta| < 90$ deg and $|\beta| < 90$ deg is convergent.

Remark: The reason that 30 deg is the critical η^* can be understood by recognizing that if $\eta^* = 30$ deg, then the maximum acceleration is $a_{s\,\text{max}} = (2V^2/L_1)\sin\eta^* = V^2/L_1$ which implies that, when saturated, the vehicle can create a circular trajectory of radius L_1. On the other hand, if $\eta^* < 30$ deg then the maximum acceleration is $a_{s\,\text{max}} < V^2/L_1$, and so the minimum turning radius will be larger than L_1. As a result, it is straightforward to construct limiting scenarios whereby the distance to the circle will exceed L_1 and the reference point on the desired path will be lost.

VI. Flight Test Results

The guidance algorithm was implemented and tested with the two UAVs constructed in the parent child unmanned air vehicle
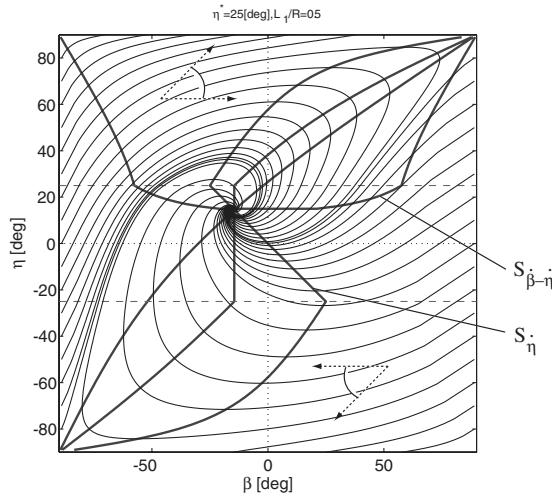
Fig. 15 Phase plot as an example case of $\eta^* < 30$ deg.

Fig. 16 Formation flight during flight test (the minivehicle is commanded to be 12 m behind and 2 m above the parent).

(PCUAV) project at MIT. In creating the required lateral acceleration, bank angle control was used in the inner loop. The associated outer-loop control bandwidth was limited by the inner-loop bank control bandwidth (2–3 rad/s) and a GPS time delay of 0.4 s. Thus with the nominal flight velocity of about 25 m/s, the choice of $L_1 = 150$ m results in the associated crossover frequency at 0.4 rad/s. The average wind condition in these flight tests was 5 ± 1 m/s, which was determined after the flights by comparing the GPS velocity and air-speed sensor measurements. Bank angles ranged up to about 20 deg magnitude, with bank angle limits at 30 deg magnitude.

The minichild vehicle shown in Fig. 16 has a wingspan of 2.54 m and its total weight, including onboard avionics, is 9.1 kg. The parent vehicle in the same figure has an outboard horizontal stabilizer (OHS) configuration. The aerodynamic and the associated stability features of this platform are in [17,18]. The vehicle has a wing span of 4.5 m and its total weight is 20 kg.

Figure 17 shows the flight data for the minivehicle using the nonlinear guidance law for path following in the lateral direction. The plot shows the two-dimensional trajectory of the minivehicle (solid line) with a commanded desired trajectory (dotted line). The small numbers along the trajectory are the flight times recorded in the onboard avionics. This plot indicates that the vehicle follows the commanded trajectory quite well. When the minivehicle flies along the circle the lateral displacement between the vehicle and the desired path remained within ± 2 m for 75% of its flight time and within ± 3 m for 96% of the flight time.

The tight trajectory tracking capability of both aircraft, as facilitated by the nonlinear guidance method, demonstrated that the
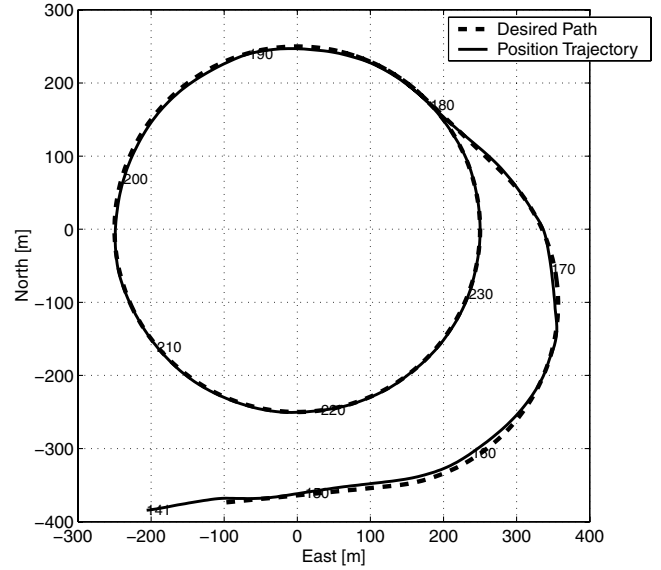

Fig. 17 Flight data of minivehicle trajectory following.

two vehicles can rendezvous from arbitrary initial positions to a configuration of precise formation flight on the same desired circular path. Figure 16 shows a photo taken from the ground during the formation flight period. During formation flight the along track separation distance command was reduced gradually by a ground station command from an initial command of 30 m, in steps, down to 12 m. During the period of the entire formation flight, the separation distance command was slowly reduced, and the minivehicle followed its command within an error of ± 2 m, for 86% of this period. Sensor errors in the onboard inertial system and wind variations are the most likely contributors to these remaining errors.

VII. Conclusions

This paper discussed a nonlinear path following guidance law that has been adapted from pure pursuit based methods, and reported flight test results using this algorithm to accurately control two UAVs in the presence of significant wind disturbances. The results in this paper extended previous linear stability analysis to demonstrate that the algorithm has an element of anticipation of the desired flight path, enabling tight tracking of curved flight trajectories. We also demonstrate asymptotic Lyapunov stability of the nonlinear guidance law for the entire state space of useful initial conditions, for all velocities, and also with saturation of lateral acceleration. The analysis shows that the nonlinear method will provide superior performance to the traditional linear technique, which occurs for the following reasons:

1) The angle η used in the guidance law serves three purposes. First it provides a heading correction. Second for small deviations from the desired trajectory it provides proportional-derivative control on cross-track error. And third it provides an anticipatory acceleration command to exactly follow a circular reference trajectory.

2) The guidance law uses the instantaneous vehicle inertial speed in the computation of the acceleration command. This kinematic factor adds an adaptive capability with respect to changes in vehicle ground speed, due to external disturbances such as wind.

Acknowledgments

References

[1] Keviczky, T., and Balas, G. J., "Software Enabled Flight Control Using Receding Horizon Techniques," AIAA Paper 2003-5671, Aug. 2003.

[2] Murray, R. M., "Trajectory Generation for a Towed Cable System Using Differential Flatness," *International Federation of Automatic Control (IFAC) World Congress*, IFAC, Oxford, U.K., 1996.

[3] Rathinam, M., and Murray, R. M., "Configuration Flatness of Lagrangian Systems Underactuated by One Control," *SIAM Journal on Control and Optimization*, Vol. 36, No. 1, 1998, pp. 164–179.

[4] Johnson, E., Calise, A., and Corban, E., "A Six Degree-of-Freedom Adaptive Flight Control Architecture for Trajectory Following," AIAA Paper 2002-4776, 2002.

[5] Nelson, D., Barber, B., McLain, T., and Beard, R., "Vector Field Path Following for Small Unmanned Air Vehicles," *Proceedings of the IEEE American Control Conference*, IEEE, Piscataway, NJ, 2006, pp. 5788–5794.

[6] Lawrence, D., "Lyapunov Vector Fields for UAV Flock Coordination," AIAA Paper 2003-6575, Sept. 2003.

[7] Niculescu, M., "Lateral Track Control Law for Aerosonde UAV," AIAA Paper 2001-0016, Jan. 2001.

[8] Amidi, O., and Thorpe, C., "Integrated Mobile Robot Control," *Proceedings of SPIE: The International Society for Optical Engineering*, Vol. 1388, March 1991, pp. 505–523.

[9] Ollero, A., and Heredia, G., "Stability Analysis of Mobile Robot Path Tracking," *Proceedings of the Institute of Electrical and Electronics Engineers/Robotics Society of Japan International Conference on Intelligent Robots and Systems*, 1995, IEEE, Piscataway, NJ, pp. 461–466.

[10] Murphy, K. N., "Analysis of Robotic Vehicle Steering and Controller Delay," *Fifth International Symposium on Robotics and Manufacturing (ISRAM)*, American Society of Mechanical Engineers, New York, 1994, pp. 631–636.

[11] Rankin, A. L., Crane, C. D., and Armstrong, D., "Evaluating a PID, Pure Pursuit, and Weighted Steering Controller for an Autonomous Land Vehicle," *Proceedings of SPIE: The International Society for Optical Engineering*, Vol. 3210, Jan. 1998, pp. 1–12.

[12] Kelly, A., "A Feedforward Control Approach to the Local Navigation Problem for Autonomous Vehicles," Carnegie Mellon University, Tech. Rept. CMU-RI-TR-94-17, 1994.

[13] Hogg, R., Rankin, A., Roumeliotis, S., McHenry, M., Helmick, D., Bergh, C., and Matthies, L., "Algorithms and Sensors for Small Robot Path Following," *Institute of Electrical and Electronics Engineers International Conference on Robotics and Automation*, IEEE, Piscataway, NJ, 2002.

[14] Jones, T., Deyst, J., and Park, S., "The Parent and Child Unmanned Aerial Vehicle System," *Unmanned Vehicle Systems International Conference*, Association for Unmanned Vehicle Systems International (AUVSI), Arlington, 2003.

[15] Blanchini, F., "Set Invariance in Control: A Survey," *Automatica*, Vol. 35, No. 11, Nov. 1999, pp. 1747–1768.

[16] Slotine, J.-J. E., and Li, W., *Applied Nonlinear Control*, Prentice–Hall, Upper Saddle River, NJ, 1991.

[17] Kentfield, J., "Upwash Flowfields at the Tails and Aircraft with Outboard Horizontal Stabilizers," AIAA No. 1998-757, 1998.

[18] Mukherjee, J., "Automatic Control of an OHS Aircraft," Ph.D. Dissertation, University of Calgary, Calgary, Alberta, Canada, 2000.